S matrix from a two-dimensional slab covered by water drops in W and J bands: Comparison of a full-wave method with measurements

Christophe Bourlier, Paul Bouquin, Alain Peden, Daniel Bourreau, Nicolas Pinel

Journal of Infrared, Millimeter, and Terahertz Waves
https://doi.org/10.1007/s10762-024-00977-y

RESEARCH

$\bar{S}$ Matrix from a Two-Dimensional Slab Covered by Water Drops in *W* and *J* Bands: Comparison of a Full-Wave Method with Measurements

Christophe Bourlier[1] · Paul Bouquin[2] · Alain Peden[2] · Daniel Bourreau[2] · Nicolas Pinel[3]

Received: 9 October 2023 / Accepted: 14 February 2024

Abstract
This paper presents a full-wave method, based on the method of moments (MoM), to calculate the $\bar{S}$ matrix from a two-dimensional complex sample in millimeter and submillimeter *W* and *J* bands. From the surface currents obtained by inverting the impedance matrix and from the Huygens principle, the reflection and transmission coefficients are computed. This allows us to obtain the four elements of the $\bar{S}$ matrix. Firstly, the method is validated from canonical samples (a dielectric slab and a stack of two dielectric slabs) by applying the well-known Fresnel coefficients. Secondly, for the *W* (75 to 110 GHz) and *J* (220 to 330 GHz) bands, a PVC slab covered by water drops is considered, for which the $\bar{S}$ matrix is compared with measurements made in quasi-optical free space. A satisfactory agreement is obtained between the measurements and the model.

Keywords Boundary integral equation · Method of moments · Millimeter and submillimeter measurements · Radome · Scattering and propagation

1 Introduction

The mm-wave and low THz bands are of use for many applications [1–3]. When operating outside, the system antennas must be protected from the environment by a radome. Water can be deposited onto the radome during rainfall events and cause

✉ Christophe Bourlier
Christophe.Bourlier@univ-nantes.fr

1 Nantes Université, CNRS, IETR (Institut d'Electronique et des Technologies numéRiques), UMR 6164, F-44000 Nantes, France

2 Lab-STICC, UMR 6285 CNRS, IMT Atlantique, technopôle Brest-Iroise, CS 83818, 29238 Brest Cedex 3, France

3 Icam Ouest, Nantes Université, CNRS, IETR, UMR 6164, F-44000 Nantes, France

detrimental effects for applications such as automotive radar [4, 5]. Free space measurements can be done to investigate the impact of the water layer deposited onto the radome through the scattering parameters ($\bar{\boldsymbol{S}}$ matrix) [6–9].

Modeling the $\bar{\boldsymbol{S}}$ matrix of such a system, both in modulus and in phase, is a challenging problem. The Fresnel coefficients [10] provide an exact analytical solution of the $\bar{\boldsymbol{S}}$ matrix by assuming a stack of smooth interfaces of infinite areas separating homogeneous dielectric media. For a more complex geometry, such as a radome covered with water drops, more complex methods must be investigated to account for the geometry profile variations. In the context of electromagnetic scattering, this issue can be solved from asymptotic or/and rigorous approaches. The asymptotic (or approximate) models are based on the introduction of simplifying assumptions, while the rigorous ones are less restrictive and can be applied for any geometry. Rigorous methods can be classified into two main families: differential equations methods, where the space is discretized from finite element method (FEM) [11, 12] or from finite difference time domain (FDTD) method [13, 14], and the integral boundary methods, where the boundaries are discretized by using the method of moments (MoM) [15, 16].

In this paper, the full-wave MoM implemented since the 1970s is an appropriate rigorous method to calculate the scattered field from a collection of dielectric scatterers assumed to be homogeneous. It converts the boundary integral equations into a linear system, in which the square impedance matrix $\bar{\boldsymbol{Z}}$ must be inverted. For a single scatterer, its size N is proportional to the number of discretized points (or facets) on the object's surface. It increases as the frequency or/and the real part of the relative permittivity of the inner medium grows. The direct solver, LU (lower-upper) decomposition, is commonly applied if the value N is moderate. For huge N, the inversion of $\bar{\boldsymbol{Z}}$ can be very time-consuming and requires a large memory space. Iterative solvers [16, 17] have been developed to solve this issue.

For several scatterers, the number N equals the sum of N_i, where N_i is the number of discretized points (or facets) on the scatterer i. This means that the size of the resulting impedance matrix increases significantly in comparison to a single scatterer. This explains why the MoM was first developed for a single two-dimensional (2D) scatterer, next for a three-dimensional (3D) scatterer, and for a collection of 2D or 3D objects. 2D means that the object geometry is invariant with respect to a direction, chosen as y (normal to the sheet) in this paper, implying that N is greatly reduced in comparison to a 3D problem. Moreover, as the number of scatterers increases, the derivation of the impedance matrix is not straightforward and remains an issue in progress, even for a 2D problem. A recent article [18] derives this expression for any 2D problem.

To our knowledge, it is the first time that the MoM is addressed to compute the $\bar{\boldsymbol{S}}$ matrix, both in modulus and in phase. For instance, the Kirchhoff diffraction theory based on strong simplifying assumptions is investigated in the recent article [8]. In this paper, to calculate the $\bar{\boldsymbol{S}}$ matrix, two distinct methods, based on the MoM, are investigated and validated by considering a dielectric slab and a stack of two dielectric slabs, for which the $\bar{\boldsymbol{S}}$ matrix is derived from the well-known Fresnel coefficients [10]. The first method is based only on the Huygens principle (currents radiation), and the second one is related to the Kirchhoff approximation (KA) combined with the

Huygens principle. Next, the two methods are tested on a PVC (plastic) covered by water drops and compared with measurements.

The W- and J-band measurement system is described in Sect. 2, and the MoM is addressed in Sect. 3. It is important to underline that this system measures the four complex elements of the $\bar{\boldsymbol{S}}$ matrix, both in modulus and in phase. Section 4 presents comparisons between experimental and simulation results, and the last section gives concluding remarks.

2 Description of the Free-Space System Setup

2.1 Experimental Setup

We use two different quasi-optical benches operating in the W (75 to 110 GHz) and J (220 to 330 GHz) frequency bands. The principle for every frequency band is the same (Fig. 1): A vector network analyzer (VNA) in a 2-port configuration produces a signal which is converted into the desired band by a frequency converter. The transmitted signal goes then through a corrugated horn illuminating a lens and propagates in free space as a Gaussian beam. In the middle of the two lenses, the sample under study is placed at the waist of the Gaussian beam. For each frequency band, different frequency converters, antennas, and lenses are dedicated. The W-band setup and the characterization method for a solid material are described in [6]. To obtain the four $\{S_{11}, S_{21}, S_{12}, S_{22}\}$ parameters ($\bar{\boldsymbol{S}}$ matrix), a through-reflect-line (TRL) calibration is performed to ensure an accurate location of the reference plane. A metal plate is used for the reflect standard, and both the lens and the antenna at port 2 are moved for the line standard.

A new calibration is performed before each set of measurements. Two phase corrections are applied to the measured $\bar{\boldsymbol{S}}$ matrix. The first one accounts for the difference between the reference plane of the TRL calibration (bottom plane in 2) and the desired plane for the $\{S_{11}, S_{12}, S_{21}, S_{22}\}$ parameters. For this correction, a phase shift, corresponding to an air layer with a thickness equal to the total thickness of the system, is applied. The second correction takes into account a possible difference between the reference plane of the TRL calibration and the actual position of the measured sample. This correction is a phase shift corresponding to an air layer with a thickness of a few tens of μm equal to a possible misplacement. It is applied to the S_{11} and S_{22} parameters. Thanks to these two corrections, a good control of the phase is achieved, and we can directly compare (both in modulus and in phase) the $\bar{\boldsymbol{S}}$ matrix measurements with the proposed theoretical model. In addition, it is important to underline that no smoothing or time-domain gating is applied to the measured data.

In the case of a dielectric slab, by comparing the measured $\bar{\boldsymbol{S}}$ matrix with an analytical model based on the Fresnel coefficients (see Appendix), the complex permittivity and the thickness can be extracted at each frequency point [6]. Throughout this study, the slab is a piece of PVC with a thickness $H = 5.01$ mm and with a complex relative permittivity

$$\epsilon_{r,\mathrm{PVC}} = 2.956 + i\,(0.0044 + 0.00023\,f)\,, \quad f \text{ in GHz}. \tag{1}$$

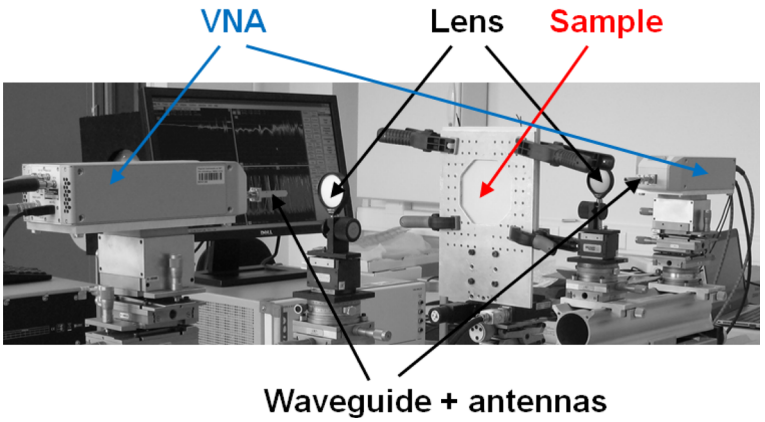

Fig. 1 Experimental setup

The dispersion of the real part is negligible (less than 1%), but the dispersion of the imaginary part must be taken into account given the wide frequency range (it matches well with a linear function).

For non-solid materials such as water, a specific pre-characterized PVC container is used, as explained in [19]. The permittivity of the non-solid material is obtained by comparing the measured and calculated $\bar{S}$ matrices of the container filled with water. The calculated $\bar{S}$ matrix is expressed in the Appendix.

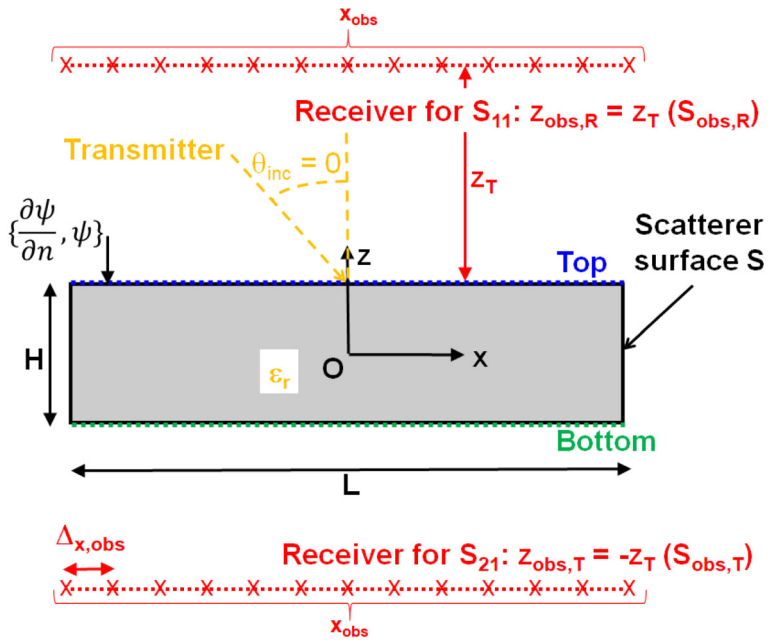

Fig. 2 Description of the geometry. The setup geometry is vertical whereas in Fig. 1, it is horizontal

In the present study, we use tap water. The water is left in the open air for a couple of days for the chlorine to be evaporated. The measured complex relative permittivity of water in the W and J bands is fitted from the following Debye model [20]:

$$\epsilon_{r,\text{Water}} = \epsilon_{r,\infty} + \frac{\epsilon_{r,0} - \epsilon_{r,\infty}}{1 - 2\pi i f \tau}. \tag{2}$$

The following parameters are obtained:

$$\begin{cases} \epsilon_{r,\infty} = 5.68,\ \epsilon_{r,0} = 66.7,\ \tau = 6.98 \text{ ps (W band)} \\ \epsilon_{r,\infty} = 5.83,\ \epsilon_{r,0} = 86.5,\ \tau = 7.51 \text{ ps (J band)} \end{cases}. \tag{3}$$

The above values depend slightly on the band because the measurements were not performed simultaneously. For the J band, the temperature was 29 °C, while it was about 22 °C for the W band.

2.2 Control of the Water Shape

From a given water volume, we first deposit water drops by using a syringe. After this first set of measurements, the water is collected again and deposited as a thin uniform film by using a polycarbonate plate to flatten it and double-sided adhesive tape as a seal (see right-hand side of Fig. 3). A surface of 80 cm^2 is delimited with tape. The total volume of water is 0.8 mL. Ten percent of the volume can be lost due to evaporation or other losses between each step. We measure the radius of the droplets with a microscope, and in order to estimate the total percent of the surface covered by water, we add colorant to the water. On the 80 cm^2 surface, 87 drops are deposited, giving a total percent of wet surface of $10.5 \pm 1\%$. Note that the drops are not perfect half-spheres, and thus, the wet surface cannot be deduced exactly from the water volume, the total surface, and the number of drops.

The uniform water layer is about 0.0875 mm thick, assuming that the water is evenly distributed below the polycarbonate plate. In order to remove the contribution of the

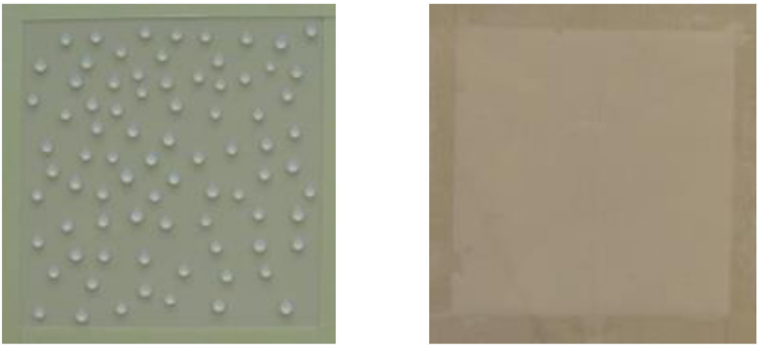

Fig. 3 Slab covered by a distribution of water drops (on the left) and by a uniform thin film (a surface of 80 cm^2 is delimited with a double-sided adhesive tape)

plate from the slab covered by the uniform water layer measurement, we characterize the plate alone by using the same procedure as explained previously for the water permittivity extraction.

To compare the measurements made on the two samples shown in Fig. 3, a theoretical model is developed in the following section.

3 Method of Moments

In the following, a variable in boldface stands for a vector ($\boldsymbol{a}$), a variable in boldface with a hat above refers to a unitary vector ($\hat{\boldsymbol{a}}$), and a variable in boldface with a bar above is a matrix ($\bar{\boldsymbol{a}}$). The method of moments (MoM) is typically applied to compute the radar cross section from objects for radar applications. In this paper, it is used to calculate the $\bar{\boldsymbol{S}}$ matrix. To our knowledge, it is the first time this method is adapted to calculate the $\bar{\boldsymbol{S}}$ matrix.

The MoM discretizes the boundary integral equations on the scatterer surfaces, the latter being assumed to be homogeneous. This transformation leads to solving the linear system $\bar{\boldsymbol{Z}}\boldsymbol{X} = \boldsymbol{b}$, where $\bar{\boldsymbol{Z}}$ is the impedance matrix (which depends on the shape of the surfaces and on the permittivities of the media), $\boldsymbol{b}$ the incident field discretized on the surfaces, and $\boldsymbol{X}$ the unknown of the problem. This vector contains the weights of the electric and magnetic surface currents, which are discretized on the surfaces. Thus, it is obtained by $\boldsymbol{X} = \bar{\boldsymbol{Z}}^{-1}\boldsymbol{b}$, requiring to invert a matrix. A conventional LU decomposition is then applied to obtain $\boldsymbol{X}$.

In this paper, a two-dimensional (2D) problem is considered in the Cartesian coordinate system (x, z). This means that the objects are invariant along the direction y and that the profile of the surface is defined by the function $z = f(x)$. For a 2D problem, the principle of MoM is addressed in [18] for several objects, while [16] gives all the details.

The size of the matrix $\bar{\boldsymbol{Z}}$ is proportional to the electrical dimensions of the geometries. Typically, for a dielectric object of complex relative permittivity ϵ_r, the sampling step along the abscissa x is set to $\Delta x = \lambda_0/[\mathrm{Re}(\sqrt{\epsilon_r})p]$, with p an integer. Typically, $p \in [10; 40]$, depending on the desired precision. The quantity $\lambda_0 = c/f$ is the wavelength in the vacuum, c is the celerity of the light in the vacuum, and f is the frequency.

To calculate the vector $\boldsymbol{b}$ (in order to solve $\bar{\boldsymbol{Z}}\boldsymbol{X} = \boldsymbol{b}$), the incident field must be known. To match with the experimental setup in order to compare with the measurements, the incident field is assumed to be a tapered Gaussian wave, which is defined for a normal incident angle as

$$\psi_{\mathrm{inc}}(x, z) = \exp(-ik_0 z)\exp\left(-\frac{x^2}{w_0^2}\right), \tag{4}$$

where w_0 is the waist and $k_0 = 2\pi/\lambda_0$ the electromagnetic wavenumber. As shown in Fig. 2, the incidence angle defined from the nadir θ_{inc} equals zero. A plane incident wave is written as $\exp(-ik_0 z)$, corresponding to the first term in the right-hand side

of Eq. 4. The second one is an attenuation term along the abscissa x controlled by the extent w_0.

Typically, $w_0 = 25$ mm and the illuminated slab abscissa $x \in [-L/2; L/2]$, where L is the slab length. In the experiment, a square surface of 80 cm^2 is used, corresponding to a side of $L \approx 92$ mm. Thus, for $x = \pm L/2$, $|\psi_{\text{inc}}(x, z)| = \exp(-x^2/w_0^2) \approx 0.034$. This means that the incident field modulus is nearly zero near the two borders of the slab, which avoids edge diffraction. In other words, the incident field "does not illuminate" the borders, which implies that the slab is nearly "infinite" from an electromagnetic point of view. This statement is crucial when we compare it with the well-known Fresnel coefficients, which assume that the illuminated slab is infinite with respect to the x direction.

The MoM computes the vector $\boldsymbol{X}$ that contains the surface currents $\psi(\boldsymbol{r})$ and their normal derivatives $\partial\psi(\boldsymbol{r})/\partial n = \boldsymbol{\nabla}\psi(\boldsymbol{r}) \cdot \hat{\boldsymbol{n}}$, with $\boldsymbol{r} = (x, z) \in S$ on the discretized points of the surface S, and $\hat{\boldsymbol{n}}$ is the normal to the surface at a given discretization point. The symbol $\boldsymbol{\nabla} = \hat{\boldsymbol{x}}\partial/\partial x + \hat{\boldsymbol{z}}\partial/\partial z$ stands for the nabla differential operator.

The MoM is applied for a given frequency. For N_f frequencies, it is applied N_f times.

3.1 Method 1: MoM

By applying the Huygens principle for the radiation of the surface currents $\{\psi, \partial\psi/\partial n\}$, the 2D scattered field is expressed as [16]

$$\psi_{\text{sca}}(\boldsymbol{r}') = \int_S \left[\psi(\boldsymbol{r})\frac{\partial g_0(\boldsymbol{r}, \boldsymbol{r}')}{\partial n} - g_0(\boldsymbol{r}, \boldsymbol{r}')\frac{\partial\psi(\boldsymbol{r})}{\partial n}\right] dS, \tag{5}$$

where $g_0(\boldsymbol{r}, \boldsymbol{r}')$ is the 2D Green function in free space, defined as

$$\begin{cases} g_0(\boldsymbol{r}, \boldsymbol{r}') = \dfrac{i}{4}\mathrm{H}_0^{(1)}\left(k_0 \left\|\boldsymbol{r} - \boldsymbol{r}'\right\|\right) \\ \dfrac{\partial g_0(\boldsymbol{r}, \boldsymbol{r}')}{\partial n} = -\dfrac{i}{4}\dfrac{\mathrm{H}_1^{(1)}\left(k_0 \left\|\boldsymbol{r} - \boldsymbol{r}'\right\|\right)}{\left\|\boldsymbol{r} - \boldsymbol{r}'\right\|}\left(\boldsymbol{r} - \boldsymbol{r}'\right) \cdot \hat{\boldsymbol{n}} \end{cases}. \tag{6}$$

In addition, the functions $\mathrm{H}_0^{(1)}$ and $\mathrm{H}_1^{(1)}$ are the Hankel functions of the first kind and zeroth order and first order, respectively, and $\boldsymbol{r}' \notin \boldsymbol{r}$ ($\boldsymbol{r} \in S$) is an arbitrary observation point of coordinates (x', z'). Knowing ψ_{sca}, the reflection $R = \{S_{11}, S_{22}\}$ and transmission $T = \{S_{21}, S_{12}\}$ coefficients must be determined. In Eq. 5, dS is an elementary line (because a 2D problem is solved) surface.

The first method, named "Method 1" or "MoM," defines the (radiated) reflection R and transmission T coefficients as

$$\begin{cases} R = S_{11} = \dfrac{\sum_{n=1}^{n=N_{\text{obs}}} \psi_{\text{sca}}(\boldsymbol{r}'_n)}{\sum_{n=1}^{n=N_{\text{obs}}} \psi_{\text{sca},R}(\boldsymbol{r}'_n)} & \boldsymbol{r}'_n \in S_{\text{obs},R} \\ T = S_{21} = \dfrac{\sum_{n=1}^{n=N_{\text{obs}}} \psi_{\text{sca}}(\boldsymbol{r}'_n)}{\sum_{n=1}^{n=N_{\text{obs}}} \psi_{\text{sca},T}(\boldsymbol{r}'_n)} & \boldsymbol{r}'_n \in S_{\text{obs},T} \end{cases} . \tag{7}$$

As shown in Fig. 2, in Eq. 7, the observation surface in reflection, $S_{\text{obs},R}$, is defined at the constant height $z = z_{\text{obs},R} = z_T \ \forall x'$ (corresponding to the location of a lens in Fig. 1) and on the reflection side ($z_{\text{obs},R} > H/2$), whereas for the transmission, $S_{\text{obs},T}$, it is defined at the constant height $z = z_{\text{obs},T} = -z_T$ but on the transmission side ($z_{\text{obs},T} < -H/2$). Typically, $z_T = 400$ mm, corresponding to the lens locations in the measurement setup. The sample is centered on ($x = 0, z = 0$). In addition, the abscissa x_{obs} of S_{obs} goes from $-L/2$ to $L/2$, with a sampling step $\Delta_{x,\text{obs}} = \lambda_0/10$ to capture the phase variations of the scattered field. From Eq. 7, R and T are averaged over x_{obs}, where N_{obs} is the number of observation points. Equation 7 also requires the knowledge of the fields in reflection, $\psi_{\text{sca},R}$, and in transmission, $\psi_{\text{sca},T}$.

To calculate $\psi_{\text{sca},R}$, the geometry is replaced by a perfectly conducting surface of length L and of center $(0, H/2)$ (slab top), where H is the slab thickness. From this new geometry, the scattered field ψ'_{sca} is computed from Eq. 5 and evaluated on the surface $S_{\text{obs},R}$, giving $\psi_{\text{sca},R} = \psi'_{\text{sca}}$ for $\boldsymbol{r}' \in S_{\text{obs},R}$. This is analog to the reflect standard applied in VNA calibration.

The calculation of $\psi_{\text{sca},T}$ is more complicated. The obvious way would be to apply Eq. 4 with $z = -z_T$ and $x' \in S_{\text{obs},T}$, but from Eq. 5, we can show that the scattered field is a cylindrical wave (in far field), meaning that its modulus is proportional to $1/\sqrt{r'}$, where $r' = \sqrt{x'^2 + z'^2}$. Since the incident field modulus does not have this behavior, the ratio between these two fields (Eq. 7) has no sense because their dimensions differ. To have a consistent approach, the relative permittivity of the slab is replaced by that of the air, which is equal to unity. This means that the scatterer is not "viewed" by the incident wave, which is similar to not considering it. Next, the resulting linear system is solved, and the scattered field is computed from Eq. 5 for $\boldsymbol{r}' \in S_{\text{obs},T}$. This is analog to the through standard applied in VNA calibration. Unfortunately, numerical results will show that this approach gives an unphysical S_{21}. From a mathematical point of view, this behavior is expected because the equivalent problem corresponds to the propagation between two points located inside a unique medium. Thus, the boundary integral equations have no sense.

To solve this issue, another approach is addressed.

3.2 Method 2: MoM Combined with KA

The second method, named "Method 2" or "MoM+KA," also applies the MoM to calculate the surface currents, but the scattered field is evaluated in a different way. By analogy with the Kirchhoff approximation (KA) or the tangent plane approximation [16], for $\boldsymbol{r} \in S$, the surface currents, computed from the MoM, can be expressed as

$$\begin{cases} \psi(\boldsymbol{r}) = (1 + R_S)\psi_{\text{inc}}(\boldsymbol{r}) \\ \dfrac{\partial \psi(\boldsymbol{r})}{\partial n} = (1 - R_S)\dfrac{\partial \psi_{\text{inc}}(\boldsymbol{r})}{\partial n} \end{cases} \quad \boldsymbol{r} \in S, \tag{8}$$

where R_S is the reflection coefficient on the surface. To be consistent with KA, the surface curvature radius (or small surface slope) must be larger than the electromagnetic wavelength λ_0. In other words, KA is not valid on the slab borders defined at $x = \pm L/2$.

By considering only $\psi(\boldsymbol{r})$, from Eq. 8, R_S is given by

$$R_S = \frac{\psi(\boldsymbol{r}) - \psi_{\text{inc}}(\boldsymbol{r})}{\psi_{\text{inc}}(\boldsymbol{r})} \quad \boldsymbol{r} \in S_{\text{Top}}, \tag{9}$$

where S_{Top} is the surface points on the slab top (blue dashed line in Fig. 2). To calculate the radiated reflection coefficient $R_{S,\text{sca}}$, the above equation must be integrated on S_{Top}. By using Eq. 5 with $\partial\psi/\partial n = 0$, we have

$$R_{S,\text{sca}}(\boldsymbol{r}') = \frac{\mathcal{L}_R(\psi) - \mathcal{L}_R(\psi_{\text{inc}})}{\mathcal{L}_R(\psi_{\text{inc}})} \quad \boldsymbol{r}' \in S_{\text{obs},R}, \tag{10}$$

where the integral operator $\mathcal{L}_R$ is expressed for any function $f(\boldsymbol{r})$ as

$$\mathcal{L}_R[f(\boldsymbol{r})](\boldsymbol{r}') = \int_{S_{\text{Top}}} f(\boldsymbol{r}) \frac{\partial g_0(\boldsymbol{r}, \boldsymbol{r}')}{\partial n} dS. \tag{11}$$

The reflection coefficient S_{11} is obtained by taking the mean value of $R_{S,\text{sca}}(\boldsymbol{r}')$ over the abscissa $\{x_{\text{obs},R}\}$, leading to

$$S_{11} = \frac{1}{N_{\text{obs}}} \sum_{n=1}^{n=N_{\text{obs}}} R_{S,\text{sca}}(\boldsymbol{r}'_n). \tag{12}$$

Using the same way for the transmission case, we obtain

$$T_{S,\text{sca}}(\boldsymbol{r}') = \frac{\mathcal{L}_T(\psi)}{\mathcal{L}_R(\psi_{\text{inc}})} \quad \boldsymbol{r}' \in S_{\text{obs},T}, \tag{13}$$

where

$$\mathcal{L}_T[f(\boldsymbol{r})](\boldsymbol{r}') = \int_{S_{\text{Bot}}} f(\boldsymbol{r}) \frac{\partial g_0(\boldsymbol{r}, \boldsymbol{r}')}{\partial n} dS. \tag{14}$$

For the transmission, it is important to underline that the integration over the scatterer surface is made only on the slab bottom (dashed green line in Fig. 2). The transmission coefficient S_{21} is therefore given by

$$S_{21} = \frac{1}{N_{\text{obs}}} \sum_{n=1}^{n=N_{\text{obs}}} T_{S,\text{sca}}(\boldsymbol{r}'_n). \tag{15}$$

Moreover, since the reference phase is defined at the slab top (position of the perfectly conducting plate introduced in the method 1), S_{21} must be defined from the slab top. As a consequence, in Eq. 13, ψ_{inc} must be multiplied by the phase correction $\exp(ik_0\text{Re}(\sqrt{\epsilon_r})H)$, where ϵ_r is the slab relative permittivity.

3.3 Calculation of S_{21} and S_{22}

The coefficients S_{11} and S_{21} are obtained when the incident wave propagates in $-z$ direction (down-going wave). The coefficients S_{12} and S_{22} are obtained when the incident wave propagates in $+z$ direction (up-going wave), coming from the below of the slab. Mathematically, it is equivalent to take the complex conjugate of the incident field and by switching $(S_{\text{Top}}, S_{\text{Bot}}) \rightarrow (S_{\text{Bot}}, S_{\text{Top}})$ and $(S_{\text{obs},R}, S_{\text{obs},T}) \rightarrow (S_{\text{obs},T}, S_{\text{obs},R})$.

4 Validation and Comparison with Measurements

The polarization of the incident wave is H (horizontal or TE), which means that the incident electric field is collinear with the y direction.

4.1 Dielectric Slab

The geometry is shown in Fig. 2. The slab length is $L = 92$ mm, and its thickness is $H = 5.01$ mm. The incident wave waist equals $w_0 = 25$ mm. The relative permittivity of the PVC slab is expressed by Eq. 1. The observation height is $z_T = 400$ mm to match the experimental setup. The sampling step Δx of the surface is $\Delta x = \lambda_0/[\text{Re}(\sqrt{\epsilon_{r,\text{PVC}}})p]$, where the integer $p = 40$. The value Δx decreases as the frequency grows (Figs. 3 and 4).

On the left, Fig. 5 plots the modulus of $\{S_{11} = S_{22}, S_{21} = S_{12}\}$ in dB scale versus the frequency (W band), whereas on the right, their phase is plotted. For S_{21}, the results calculated from the MoM (method 1) are not represented because values much larger than one occur. This unphysical behavior comes from the calculation of the incident field (numerator of Eq. 7). Different ways have been tested to calculate it, but without any success. In the following, to predict S_{21}, only the method "MoM+KA" will be kept on.

As we can see in Fig. 5, a good agreement is obtained between the reference solution (generalization of the Fresnel coefficients to a slab addressed in Appendix) and the

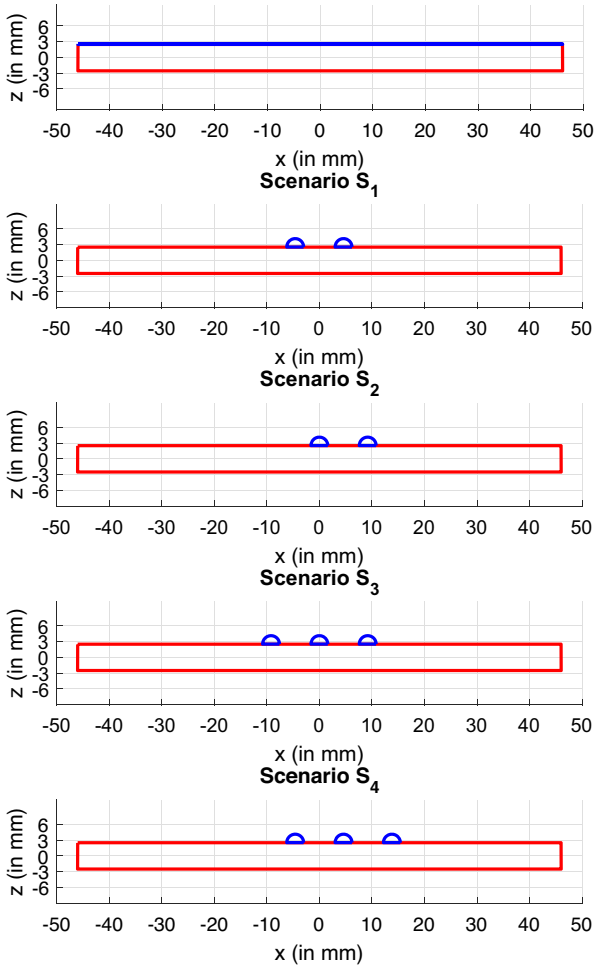

Fig. 4 Upper left panel: case of two dielectric slabs. The top one (blue line) is tap water. The bottom one (red line) is PVC of thickness 5.01 mm. Their length is 92 mm. Other panels: A PVC slab covered by water drops; scenarii 1, 2, 3, and 4 of Table 1. The drops are assumed to be infinite along the y direction

methods 1 (except for S_{21}) and 2, both in phase and in modulus. As expected, the modulus nearly follows a periodic function, due to the interferences between the direct reflected ray (for S_{11}) and those emanating from the transmission through the slab. The period Δf can be evaluated as

$$\Delta f = \frac{c}{2\bar{n}H}, \bar{n} = \frac{1}{N_f}\sum_{i=1}^{i=N_f} \mathrm{Re}\left(\sqrt{\epsilon_r(f_i)}\right), \tag{16}$$

where $c = 3 \times 10^8$ m/s and $\bar{n}$ is the mean refraction index of its real part over the frequency band. From Eq. 1, $\bar{n} \approx 1.72$ and $\Delta f \approx 17.42$ GHz, which is consistent with

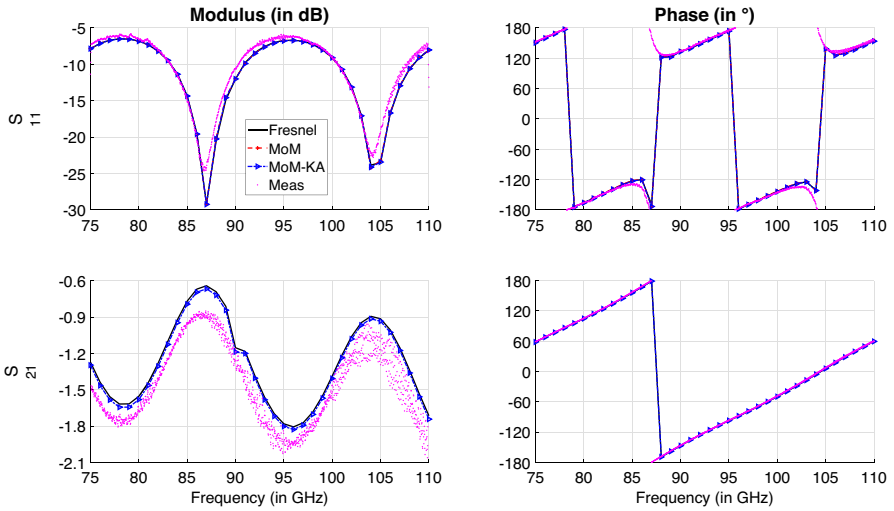

Fig. 5 On the left, modulus of $\{S_{11} = S_{22}, S_{21} = S_{12}\}$ in dB scale versus the frequency (W band). On the right, the corresponding phase. The geometry is shown in Fig. 2, where $L = 92$ mm, $H = 5.01$ mm, and $w_0 = 25$ mm

Fig. 5. In addition, the plastic skin depth goes from 50.2 to 101.1 mm from 75 to 110 GHz, which is much larger than the slab thickness $H = 5.01$ mm. This explains that the amplitudes of the local maxima do not change significantly with the frequency. In addition, in Fig. 5, the measurements (legend "Meas") match well with the reference solution.

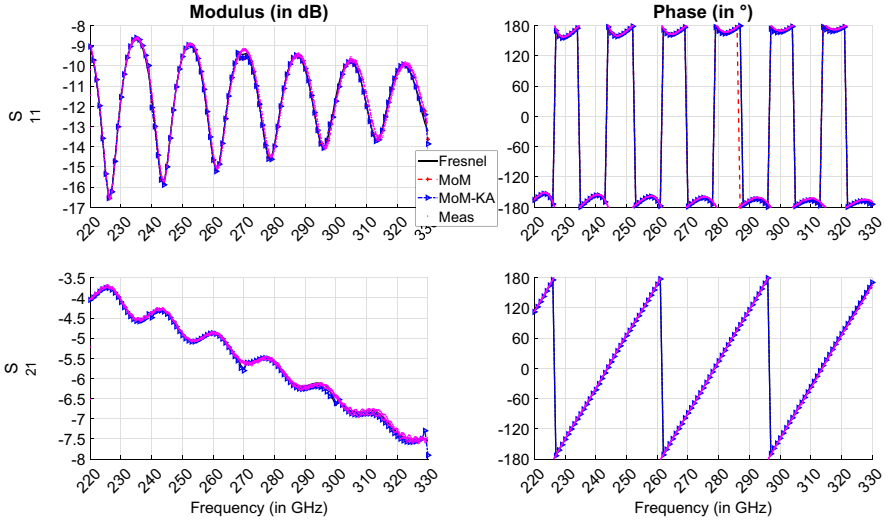

Fig. 6 Same variations as in Fig. 5, but the frequency band is J

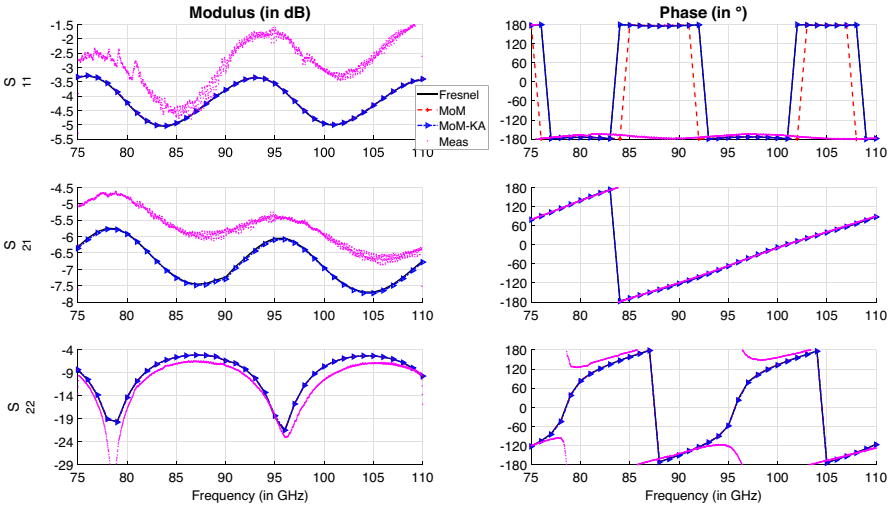

Fig. 7 On the left, modulus of $\{S_{11}, S_{21} = S_{12}, S_{22}\}$ in dB scale versus the frequency (W band). On the right, the phase. The geometry is shown in Fig. 4, where $L = 92$ mm, $H_{\text{Top}} = 0.0875$ mm (tap water), $H_{\text{Bot}} = 5.01$ (PVC) mm, and $w_0 = 25$ mm

Figure 6 plots the same variations as in Fig. 5, but the frequency band is J. As we can see, the results obtained from the two numerical methods (except for S_{21} of "Method 1") and from the measurements match well with those of the reference solution.

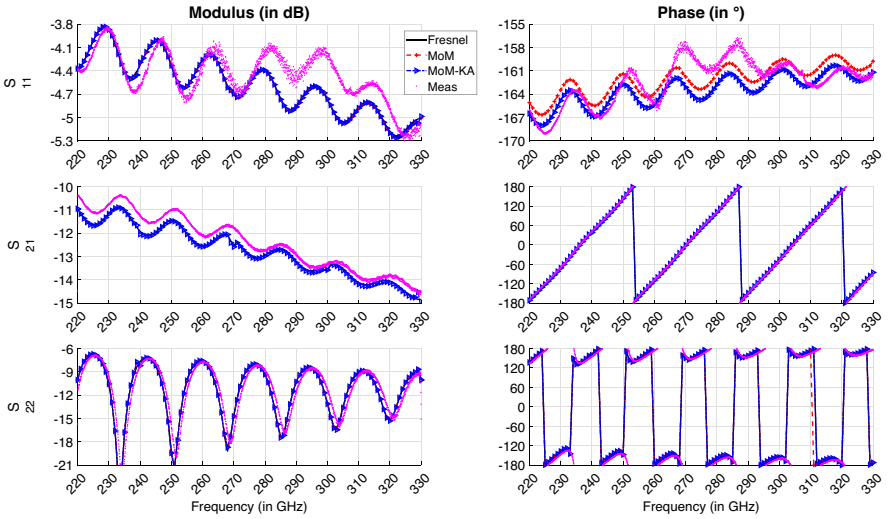

Fig. 8 Same variations as in Fig. 7, but the frequency band is J ($H_{\text{Top}} = 0.104$ mm)

4.2 Slab Covered by a Constant Thickness Water Film

We consider two dielectric slabs depicted in Fig. 4, upper panel. The bottom one is shown in Fig. 2 (previous subsection, tap water of relative permittivity given by Eq. 2), and the second one is located above, with the same length $L = 92$ mm and with thickness 0.0875 mm for the W band (and 0.104 mm for the J band). The transmission coefficient $S_{21} = S_{12}$ is calculated only from the method "MoM-KA."

On the left, Fig. 7 plots the modulus of $\{S_{11}, S_{21} = S_{12}, S_{22}\}$ versus the frequency (W band), whereas on the right, their phase is plotted. Figure 8 plots the same variations as in Fig. 7, but the frequency band is J. As we can see, the results of the two numerical methods (MoM and MoM-KA) match well with the reference solution, both in modulus and in phase. In addition, the measurements are in agreement with the reference solution, except for the S_{22} phase and for the W band. It may be caused to an experimental problem due to an uncertainty in the measured phase definition.

These comparisons (modulus and phase) allow us to validate methods 1 (except for S_{21} and S_{12}) and 2 and also show that the measurements are in agreement with the reference solution.

4.3 Slab Covered by Water Drops

From the experimental setup described in Section 2, this section presents the $\bar{\boldsymbol{S}}$ matrix for a plastic slab, as shown in Fig. 2, covered by water drops. The main issue is to reproduce the geometry (Fig. 3) of the experimental setup. First, it is important to underline that the MoM deals with a 2D problem, which means that the geometry is invariant along the y direction. In practice, it is not the case.

The following parameters are known:

- $p_S \approx 11\%$ is the percentage of the surface covered by water.
- $v_{\text{Water}} \approx 0.86$ ml is the total water volume.
- $S_{\text{Tape}} \approx 80$ cm^2 ($\approx L^2$) is the area delimited by the tape.
- $n_D = 87$, the number of water drops.

Assuming that the drops have half-ellipsoid shapes of semi-axes $\{a_i, b_i = a_i, c_i\}$ (i goes from 1 to n_D), one has (mean total area of n_D drops in the plane (x, y) is $n_D \pi \bar{a}\bar{b} = n_D \pi \bar{a}^2$)

$$\bar{a} = \sqrt{\frac{10^{-2} p_S S_{\text{Tape}}}{\pi n_D}} \approx 1.81 \text{ mm}, \tag{17}$$

and (mean total volume of n_D drops is $2 n_D \pi \bar{a}\bar{b}\bar{c}/3 = 2 n_D \pi \bar{a}^2 \bar{c}/3$)

$$\bar{c} = \frac{3 v_{\text{Water}}}{2\pi n_D \bar{a}^2} \approx 1.45 \text{ mm}, \tag{18}$$

where $(\bar{a} = \bar{b}, \bar{c})$ are the mean values of $\{a_i, b_i\}$, respectively. These values are consistent with those obtained experimentally. With respect to the x and y directions, assuming that the spacing d_D between two consecutive drops (defined from their

center) is equal, the mean spacing is

$$\bar{d}_D = \frac{\sqrt{S_{\text{Tape}}}}{\lfloor\sqrt{n_D}\rfloor + 1} \approx 9.2 \text{ mm}, \tag{19}$$

where the symbol $\lfloor$ stands for the integer part.

The incident field is a tapered wave given by Eq. 4, meaning that its modulus depends on the abscissa x. In other words, the drops are not uniformly illuminated. Like in [8], the measurements show that the $\bar{\boldsymbol{S}}$ matrix is more sensitive to the wet area (in the plane (x, y)) than the water volume. To account for this dependence, the illuminated wet surface S_{Ill} is defined as follows:

$$S_{\text{Ill}} = L \int_{-L/2}^{+L/2} |\psi_{\text{inc}}(x, z)|\, u(x) dx, \tag{20}$$

where $u(x)$ (dimensionless) is a window function.

If a uniform water film of constant thickness H_{Water} is considered, that is $u(x) = 1$ for $x \in [-L/2; L/2]$, 0 otherwise, then

$$S_{\text{Ill},0} = L \int_{-L/2}^{+L/2} e^{-\frac{x^2}{w_0^2}} dx = L w_0 \sqrt{\pi} \text{erf}\left(\frac{L}{2w_0}\right), \tag{21}$$

where erf is the error function. If $w_0 \gg L$, which corresponds to an incident wave assumed to be plane, then $S_{\text{Ill},0} \to L^2$, the area of the water film with respect to the x and y directions. For $w_0 = 25$ mm and $L = 92$ mm, $S_{\text{Ill},0} = 0.48L^2$, which implies that 48% of the wet surface is "illuminated."

For a single water drop of elliptical shape (a, c) (semi-minor and semi-major axes, respectively) and of center $(x_D, z_D = H/2)$, $S_{\text{Ill},D}$ is

$$\begin{aligned} S_{\text{Ill},D} &= c \int_{-a}^{+a} e^{-\frac{(x-x_D)^2}{w_0^2}} dx \\ &= \frac{w_0 c \sqrt{\pi}}{2} \left[\text{erf}\left(\frac{a + x_D}{w_0}\right) + \text{erf}\left(\frac{a - x_D}{w_0}\right)\right]. \end{aligned} \tag{22}$$

Table 1 Parameters of the water drops

Parameters	S_1	S_2	S_3	S_4
n_D	2	2	3	3
a_i (mm)	1.6	1.6	1.6	1.6
b_i (mm)	1.6	1.6	1.6	1.6
x_{D_i} (mm)	{−4.6;4.6}	{0;9.2}	{−9.2;0;9.2}	{−4.6;4.6;13.8}
$r_{S_{\text{Ill}},D}$ (%)	15.2	14.7	21.5	20.9

v_D is the water drop volume

The ratio, in percent, of the illuminated surface is defined as

$$r_{S_{\rm III}} = 100 \frac{S_{\rm III},\, D}{S_{\rm III,0}}. \tag{23}$$

Equation 20 can easily be generalized to a 3D problem. From the values obtained in Eqs. 17, 18, and 19, an array of $n_D = 87$ half-ellipsoids having a spatial periodicity $\bar{d}_D$ with respect to the x and y directions (panel on the left of Fig. 3) is generated. We find numerically

$$r_{S_{\rm III}} = 13.7\%. \tag{24}$$

The values listed in Eqs. 17, 18, and 19 allow us to select values in agreement with the experimental setup. Four scenarii shown in Fig. 4 are obtained, and their parameters are listed in Table 1. The numerical values of $r_{S_{\rm III},D}$ and $r_{V_{\rm III},D}$ (Eq. 22 with $L = 92$ mm) are also reported.

For the four scenarii, the horizontal distance separating the drops from their center is a constant equal to 9.2 mm. In addition, the semi-major and minor-axes of the drops are constant and $a_i = b_i = 1.6$ mm. For scenarii 1 and 2, $n_D = 2$, whereas for scenarii 3 and 4, $n_D = 3$. For scenarii 1 and 3, the drops are centered on $x = 0$, whereas for scenarii 2 and 4, they are shifted to the right of a horizontal distance of 4.6 mm. As expected, the value of $r_{S_{\rm III},D}$ increases with n_D and slightly increases when the drops are centered.

On the left, Fig. 9 plots the modulus of $\{S_{11}, S_{21} = S_{12}, S_{22}\}$ in dB scale versus the frequency (W band) and on the right, their phase. The parameters $\{S_{11}, S_{22}\}$ are computed from the MoM, whereas S_{21} is computed from the MoM-KA. Figure 10 plots the same variations as in Fig. 9, but for the J frequency band.

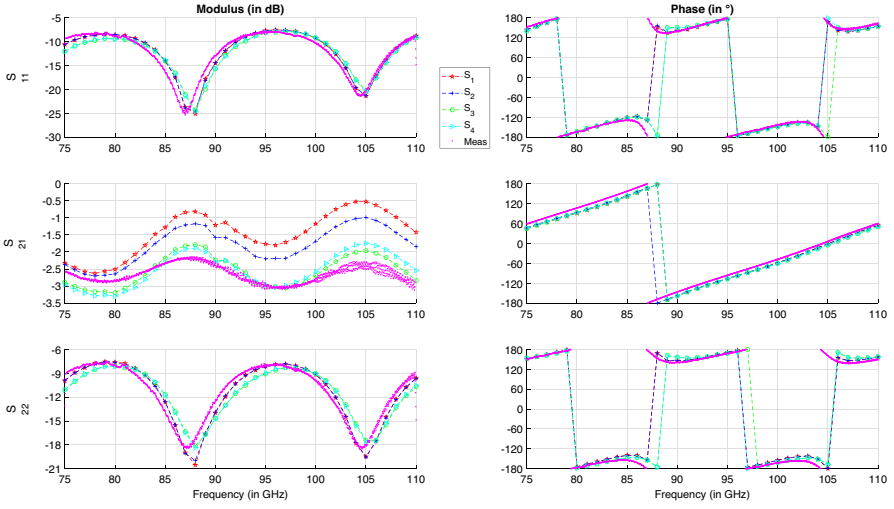

Fig. 9 On the left, modulus of $\{S_{11}, S_{21} = S_{12}, S_{22}\}$ in dB scale versus the frequency (W band). On the right, the phase. The four scenarii $\{S_i\}$ are depicted in Fig. 4

As we can see in Fig. 9, for $|S_{11}|$, the difference between the MoM results and the measurements is of the order of 1–2 dB, and the measured minima are slightly shifted toward a lower frequency. As the frequency increases, the difference diminishes, also exhibited in Fig. 10 (for the modulus, the y-scale differs in Figs. 9 and 10). In addition, the MoM results are nearly the same for the four scenarii, since the scattered field is less sensitive to the locations of the water drops. They are "seen" as the mean phenomenon only related to the wet surface, which is nearly the same for the four scenarii. For $|S_{22}|$, a similar conclusion is drawn, and we can observe that the agreement with the measurement is better for the scenarii 1 and 2. Moreover, in Fig. 10, the measurements match well for S_{22} (modulus and phase), and the MoM results nearly no longer depend on the scenario. For the phase of S_{11}, Fig. 9 exhibits a good agreement between the measurements and the MoM results, except for near the minimum locations of $|S_{11}|$.

For S_{11} and S_{22}, the MoM and MoM+KA results (not shown here) are nearly the same with a maximum difference smaller than 0.5 dB for the modulus. Concerning S_{21}, since the dynamics of $|S_{21}|$ over the frequency band is lower than those of $|S_{11}|$ and $|S_{22}|$, the differences are more visible. Nevertheless, for the scenarii 1, 2 and 4, they do not exceed 1–2 dB.

For the two frequency bands and for the full $\bar{\boldsymbol{S}}$ matrix, scenario 2 is the best candidate to reproduce the measurements both in phase and in modulus. This case corresponds to the $r_{S_{\mathrm{III}}}$ closest value (14.7%) from the measured percent of wet surface (10.5%). The main reason that could explain this difference is that the drops are assumed to be infinite along the y axis which produces more wet surface than the measurement.

In conclusion, the 2D geometrical parameters of water drop shapes were well chosen to reproduce the 3D geometry, especially scenario 2. An additional criterion is introduced to quantify the percentage of the illuminated wet surface defined in Eq. 20.

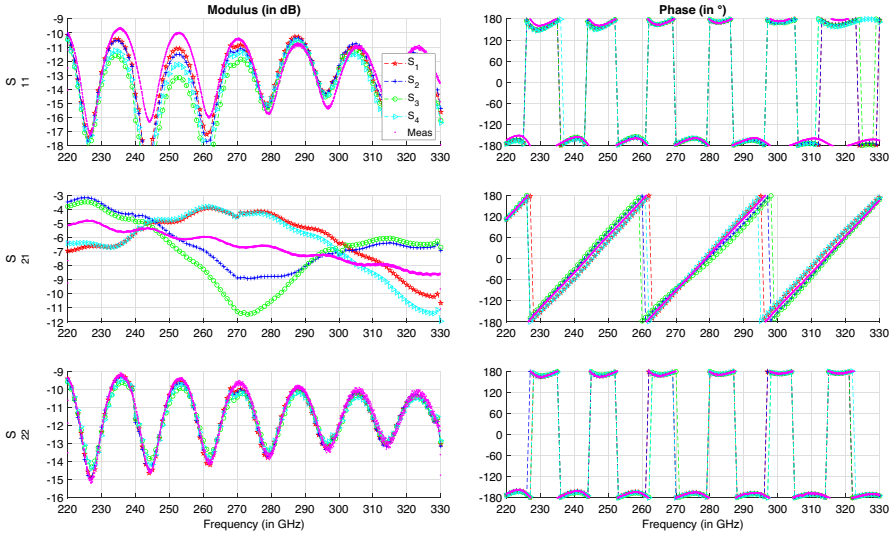

Fig. 10 Same variations as in Fig. 9, but for the J frequency band

5 Conclusion

This paper presented the full-wave MoM to calculate the three elements $\{S_{11}, S_{21} = S_{12}, S_{22}\}$ of the $\bar{S}$ matrix in W and J frequency bands and by assuming a 2D geometry. The MoM has been validated on a dielectric slab and on a stack of two dielectric slabs. Comparisons with measurements showed a very good agreement both in modulus and in phase. Moreover, the MoM results were compared with measurements, done on a 3D PVC slab covered by a distribution of water drops, for which a satisfactory agreement was obtained. To reproduce an equivalent 2D geometry, the drop water shapes and their distribution were determined and a criterion on the illuminated wet surface was defined. It must be of the same order for a 3D geometry and its 2D equivalent.

Appendix. Generalized Fresnel coefficients of a slab

To validate the two numerical methods based on the MoM, the Fresnel coefficients generalized to a slab are addressed in this Appendix. They are expressed as [10]

$$\begin{cases} R_C = \dfrac{r_{12} + r_{23}e^{2i\phi}}{1 + r_{12}r_{23}e^{2i\phi}} \\ T_C = \dfrac{t_{12}t_{23}e^{i\phi}}{1 + r_{12}r_{23}e^{2i\phi}} \end{cases}, \tag{A1}$$

where $\phi = k_0 H n_2 \cos\theta_2$, $n_2 = \sqrt{\epsilon_r}$, $\cos\theta_2 = \sqrt{1 - \sin^2\theta_2}$, $\sin\theta_2 = \sin\theta_1/n_2$. Moreover, the Fresnel coefficients are defined as

$$r_{ij} = \begin{cases} \dfrac{n_j \cos\theta_i - n_i \cos\theta_j}{n_j \cos\theta_i + n_i \cos\theta_j} & \text{V polarisation} \\ \dfrac{n_i \cos\theta_i - n_j \cos\theta_j}{n_i \cos\theta_i + n_j \cos\theta_j} & \text{H polarisation} \end{cases}, \tag{A2}$$

and

$$t_{ij} = \begin{cases} \dfrac{2n_i \cos\theta_i}{n_i \cos\theta_j + n_j \cos\theta_i} = \dfrac{n_i}{n_j}\left(1 + r_{ij}\right) & \text{V polarisation} \\ \dfrac{2n_i \cos\theta_i}{n_i \cos\theta_i + n_j \cos\theta_j} = 1 + r_{ij} & \text{H polarisation} \end{cases} \tag{A3}$$

with $n_1 = n_3 = 1$, the air refraction index and $n_2 = \sqrt{\epsilon_r}$ the one of the slab. We can note that $r_{23} = -r_{12}$. For the simulations, $\theta_1 = \theta_{\text{inc}} = 0$, which implies that

$$\begin{cases} R_{C_0} = \pm\dfrac{\rho\left(1 - e^{2i\phi_0}\right)}{1 - \rho^2 e^{2i\phi}} \\ T_{C_0} = \dfrac{\left(1 - \rho^2\right)e^{i\phi_0}}{1 - \rho^2 e^{2i\phi}} \end{cases}, \quad \rho = \frac{1 - \sqrt{\epsilon_r}}{1 + \sqrt{\epsilon_r}} \text{ and } \phi_0 = k_0 H n_2. \tag{A4}$$

where the plus sign refers to the H polarization and the minus sign to the V polarization.

By convention, the imaginary part of the relative permittivity is chosen as positive (see Eqs. 1 and 2), which implies in Eq. A1 that the sign of the phase terms, $e^{i\phi}$ and $e^{2i\phi}$, is positive to ensure an attenuation of the intensity.

Author Contribution Prof. Christophe Bourlier (C.B.) wrote the paper and developed the modeling based on the Method of Moments (MoM). Drs. Paul Bouquin, Alain Peden, and Daniel Bourreau did the measurements to compare with the MoM results. Dr. Nicolas Pinel helped C.B. on the theoretical part.

Availability of Data and Materials Not applicable

Declarations

Ethical Approval Not applicable

Conflict of Interest The authors declare no competing interests.

References

1. H.-J. Song and T. Nagatsuma, Present and future of terahertz communications, *IEEE Transactions on Terahertz Science and Technology*, vol. 1, no. 1, pp. 256–63, 2011.
2. V. Degli-Esposti, F. Fuschini, H. L. Bertoni, R. S. Thoma, T. Kurner, X. Yin, and K. Guan, Millimeter-wave and terahertz propagation, channel modeling, and applications, *IEEE Access, Special Section Editorial*, vol. 9, pp. 67,660–67,666.
3. I. F. Akyildiz, J. Miquel, and C. Han, TeraNets: ultra-broadband communication networks in the terahertz band, *IEEE Wireless Communications*, vol. 21, no. 4, pp. 130–35, 2021.
4. S. Zang, M. Ding, D. Smith, P. Tyler, T. Rakotoarivelo, and M. A. Kaafar, The impact of adverse weather conditions on autonomous vehicles: How rain, snow, fog, and hail affect the performance of a self-driving car, *IEEE Vehicular Technology Magazine*, vol. 14, no. 2, pp. 103–111, 2019.
5. J. Gong, M. Li, and M. Zhang, Material testing and optimum thickness calculation for automotive millimeter wave radar radome. Nanjing, China: International Conference on Microwave and Millimeter Wave Technology (ICMMT), 2021.
6. D. Bourreau, A. Peden, and S. Le Maguer, A quasi-optical free-space measurement setup without time-domain gating for material characterization in the w-band, *IEEE Trans. Instrumentation and Measurement*, vol. 55, no. 6, pp. 2022–28, 2006.
7. N. Chen, R. Gourova, O. Krasnov, and A. Yarovoy, The influence of the water-covered dielectric radome on 77 GHz automotive. European Radar Conference, 2017.
8. F. Norouzian, R. Du, E. G. Hoare, P. Gardner, C. Constantinou, M. Cherniakov, and M. Gashinova, Low-THz transmission through water-containing contaminants on antenna radome, *IEEE Transactions on Terahertz Science and Technology*, vol. 8, no. 1, pp. 63–75, 2018.
9. X. Liu, L. Gan, and B. Yang, Millimeter-wave free-space dielectric characterization, *Measurement*, vol. 179, p. 109472, 2021.
10. J. A. Kong, *Electromagnetic Wave Theory*. Cambdrige, Massachusetts: EMW Publishing, 2005.
11. J. Jin, *The Finite Element Method in Electromagnetics*, J. Wiley and Sons, Eds., 1993.
12. J. L. Volakis, A. Chatterjee, and L. C. Kempe, *Finite Element Method for Electromagnetics*, I. Press, Ed., 1998.
13. K. S. Yee, Numerical solution of initial boundary value problems involving Maxwell's equations in isotropic media, *IEEE Transactions on Antennas and Propagation*, vol. 14, no. 3, pp. 302–307, 1966.
14. J. B. Cole and S. Banerjee, *Computing the flow of light: Nonstandard FDTD methodologies for Photonics Design*. SPIE Press Book, 2017.
15. R. F. Harrington, *Field Computation by Moment Method*. New York: Macmillan, 1968.
16. C. Bourlier, N. Pinel, and G. Kubické, *Method of moments for 2D scattering problems. Basic concepts ans applications*, ser. Focus Series. London, UK: ISTE Ltd, John Wiley & Sons, Inc., 2013.

17. W. C. Gibson, *The Method of Moments in Electromagnetics*, Chapman and Hall/CRC, Eds., London, 2008.
18. C. Bourlier, Rough layer scattering filled by elliptical cylinders from the Method of Moments combined with the Characteristic Basis Function method and the Kirchoff approximation, *Journal of the Optical Society of America A*, vol. 38, no. 10, pp. 1581–1593, 2021.
19. D. Bourreau and A. Peden, Solid and non-solid dielectric material characterization for millimeter and sub-millimeter wave applications. Utrecht, Netherlands: IEEE: 50th European Microwave Conference (EuMC), Jan. 2021, pp. 909–912.
20. G. A. Liebe, H. J. abd Hufford and T. Manabe, A model for the complex permittivity of water at frequencies below 1 THz, *International Journal of Infrared and Millimeter Waves*, vol. 12, no. 7, pp. 659–675, 1991.